Sensors & Actuators: B. Chemical 366 (2022) 131945

Contents lists available at ScienceDirect

Sensors and Actuators: B. Chemical

journal homepage: www.elsevier.com/locate/snb

Confined adsorption within nanopatterns as generic means to drive high adsorption efficiencies on affinity sensors

Matteo Beggiato [a,b], Rishabh Rastogi [a], Christine Dupont-Gillain [c], Sivashankar Krishnamoorthy [a,*]

[a] MRT Department, Luxembourg Institute of Technology, 41, Rue du Brill, Belvaux L-4422, Luxembourg
[b] Doctoral School in Science and Engineering (DSSE), Faculty of Science, Technology and Medicine (FSTM), University of Luxembourg, Belval, Luxembourg
[c] Institut de la Matière Condensée et des Nanosciences, Faculté des Bioingénieurs, Université catholique de Louvain, Place L. Pasteur, 1 bte L4.01.10, 1348 Louvain-la-Neuve, Belgium

ARTICLE INFO

Keywords:
Nanopattern
Adsorption
Self-assembly
Quartz crystal microbalance
Biosensor
Nanoparticle

ABSTRACT

Miniaturization of the sensor active areas to length scales of the order of the analyte has been sought as means to reduce device footprints, and to capitalize on the novel optical and electronic enhancements that arise at this scale. However, little is known on what to expect of the sensor behaviour if the sensor footprints are shrunk to the dimensions of the order of analyte themselves. Our results demonstrate the densities and kinetics of adsorption of analyte to significantly increase with decrease in the sensor footprints to dimensions of the order of few multiples of analyte dimensions. Such increase is found to be generic, irrespective of the nature of interactions that drive adsorption, exhibiting qualitative similarity for electrostatic adsorption of nanoparticles, chemisorption of primary oligonucleotides, or complementary base pairing with target nucleotides. The carryover of these benefits onto a macroscopic sensor however requires high density nanopatterns exhibiting significant fill factors withtout compromising inter-feature isolation. The impact of feature dimensions, pattern fill factors, analyte concentrations, presence of convective flow, or the density of receptors are investigated using quantitative and real-time measurements of the nanostructure-analyte interactions using nanopatterned QCM sensors. The results indicate significant opportunities for rational design of nanopatterned macroscopic sensors, as well as nanoscopic sensors with sensor active areas of the order of analyte dimensions, e.g., electromagnetic hot-spots, or nanowire sensors.

1. Introduction

Spatial confinement of adsorption processes to tiny spaces of the order of few multiples of adsorbate dimensions is naturally encountered in sensing devices that deploy nanoscale components, e.g. transport via nanopores, [1] adsorption into metallic nanogaps that act as electromagnetic hot-spots, [2] or adsorption to nanowires in electronic sensors. [3] The dimensionality of the adsorption features have been theoretically been shown to impact the outcome of adsorption. [4] Zero-dimensional (0D) features were found to enhance sensitivity and response time as compared to 1D or 2D features. [3] Sutherland et al. showed an increase in the density of adsorption of laminin to antibody functionalized binary nanopatterns of circular features with feature width of 124 nm obtained by colloidal lithography. The study attributed the outcome to potential impact of nanopatches towards enhancing the availability of laminin binding regions, and reduced degree of protein denaturation. [5] Valsesia et al. produced a binary pattern of COOH nanodomes in a poly(ethylene oxide) anti-fouling matrix at different lattice constant and nanofeature diameter while keeping the surface area constant at 5%. The immobilization of receptor antibodies human-IgG was followed by Fab specific anti-human IgG. Although the study has shown improvements in terms of limit of detection (LoD) and antibody binding activity on nanopatterned surface, it is unclear whether the observed effects could be traced back to the geometric parameters. [6,7] In the same year, Krishnamoorthy et al. showed stochastic arrangement of mercaptohexadecanoic acid nanopatches (fouling) in ethylene glycol matrix (anti-fouling) with the fouling areas reaching around 10% of total surface. They found that the nanopatterned substrate increased the antigen binding capacity (ABC) by inducing a favourable antibody orientation. Their investigations showed an increase of 120% in ABC of confining nanopatterned interface as compared to unpatterned counterparts. [8] More recently, Špačková

* Corresponding author.
E-mail address: sivashankar.krishnamoorthy@list.lu (S. Krishnamoorthy).

https://doi.org/10.1016/j.snb.2022.131945
Received 4 January 2022; Received in revised form 2 April 2022; Accepted 21 April 2022
Available online 25 April 2022

et al. systematically studied the nanopatterns performance with the perspective of improving mass transport efficiency in SPR biosensors. [9] A combination of theoretical modelling as well as empirical evidences, led to the conclusion that limiting the adsorption areas to just few isolated features helps to enhance analyte mass transport to the sensor surface. [9] A theoretical model from Lynn et al. disclosed the advantages of rationally designing nanopatterned interface to maximise surface-analyte interactions from the analyte transport point of view. Although small nanofeature dimensions and low fill factors have been found to provide the best performance in terms of analyte flux towards sensing regions, they would also reduce the global surface densities, rendering signal transduction a challenge for sensors with macroscopic footprints. [10] Interestingly, in a recent instance different from biosensing context, the spatially confined adsorption to nanoscale catalysts was found to enhance the performance in hydrogen gas sensing. [11] Despite these earlier investigations, there are significant gaps in experimental understanding of the impact of confining adsorption events to lengthscale of few multiples of the adsorbate dimensions, with regards, the degree of confinement, effect of fill factors, and the presence of microfluidic flow on the adsorption outcomes. It is also unclear if the impact of the nanopattern would be dependent on the nature of adsorption, or the type of adsorbate.

In the current work we investigate the impact of nanopattern adsorption on two different adsorbates, viz. gold nanoparticles (AuNPs) and oligonucleotides. The comparable dimensions of AuNPs with single strand oligonucleotides makes them a simplistic physical model to study the adsorption process. [12] Understanding the nanopatterned attachment of nanoparticles to the surface is also attractive due to the electronic, optical and catalytic properties of the resulting assemblies, that can be leveraged to improve performance in different applications, e.g., flash memories, catalysts, plasmon-enhanced spectroscopic sensing of molecular analytes. Metal nanoparticles assemblies have also been successfully employed as tags in colorimetric, spectroscopic bioassays as well as enablers to enhance signal to noise ratio in mass [13] or refractive index sensors. [14] A rational understanding of the impact of nanopattern geometry on the NPs adsorption would benefit outcome-driven design of high performing sensors. [15,16] Additionally, gold nanoparticles offer the advantage of being easily characterized using electron or scanning probe microscope. To the best of our knowledge, there has been no investigations in literature addressing the impact of nanopattern characteristics on the outcome of nanoparticle assemblies, and their comparison with biomolecular adsorption in a manner that isolates and addresses the impact of the different contributing variables.

Realization of nanoscale areas that effectively confines adsorption events within pre-determined features down to molecular resolutions still represents a significant challenge. Different techniques have been used for nanopatterning of biological receptors on surface, including self-assembly based nanolithography, [17] porous alumina, [18] electron beam or nanoimprint lithography, [19,20] and AFM based methods. [21] While Scanning Probe Microscopy (SPM) or Electron Beam Lithography (EBL) techniques can address formation of such patterns, the resulting patterns span an area too small to enable investigation of adsorption density and kinetics using real-time analysis tools such as quartz crystal microbalance (QCM), surface plasmon resonance (SPR), surface acoustic wave (SAW) devices or ellipsometry. Techniques such as nanoimprint lithography can support large area fabrication of highly resolved nanoscale features, although it suffers from poor pattern integrity during replication of features separated by only a few nanometers. The latter is inevitable when high pattern fill factors are sought. Nanopatterning using self-assembly based techniques such as porous alumina, colloidal lithography, or block copolymers has been used to deliver large area patterns at low cost. Block copolymers offer significant process flexibility in delivering nanopatterns with lengthscales approaching molecular resolutions, while also allowing an orthogonal control over geometric variables. [22,23] However, none of these techniques have been leveraged so far, to study the impact of spatially selective adsorption to highly resolved nanopatterns, on the binding response of nanoparticles, or biomolecules. Here we demonstrate high density nanopatterns, with fill factors up to 61%, with orthogonal control over size, and fill factors, that are shown to effectively confine adsorption to the features of the nanopattern. Investigation of the impact of the nanopattern characteristics in the presence and absence of flow, on the comparison of the outcomes for adsorption of nanoparticle and oligonucleotides show rare findings of high interest and importance for the design of nanopatterned biosensors.

2. Materials and methods

2.1. Materials

Gold-coated quartz crystals (nominal frequency of 5 MHz, AT-cut and with 14 mm diameter) were purchased from Quartzpro (Järfälla, Sweden). Gold-coated SPR sensors were purchased from Technex (Wormerveer, Netherlands). Reactive Ion Etching (Plasmatherm 790, St. Petersburg, FL, USA) was used for sample cleaning, alternatively a UV-ozone was available from Jelight Company Inc. (Irvine CA, USA). Poly (styrene-*block*-2-vinyl pyridine) block copolymer was available in three different molecular weights: 248 kDa-*b*-195 kDa (System A), 55 kDa-*b*-50 kDa (System B) and 195 kDa-*b*-165 kDa (System C) they were obtained from Polymer Source Inc (Montreal, Canada). 4-aminothiophenol (4-ATP), 4-vinylpyridine thiol (4-VPT), tris(2-carboxyethyl)phosphine hydrochloride (TCEP), Sodium chloride (NaCl), 6-mercapto-1-hexanol (MCH) and tetrachloroauric(III) acid ($HAuCl_4.3\ H_2O$) were purchased from Sigma-Aldrich. Spectroscopic grade m-xylene, ethanol and acetone were obtained from Sigma-Aldrich. Phosphate-Buffered Saline (PBS) and bovine serum albumin (BSA) solution (10x concentration) were purchased from R&D System (Abingdon, UK). m-PEG6-thiol (CH_3-EG_6-SH, OEG) was obtained from BroadPharm (San Diego, CA, USA). Water was filtered through a purification system (Milli-Q, Merck) and used immediately after. Nuclease-free water and IDTE (10 mM Tris, 0.1 mM EDTA) buffer were purchase from Integrated DNA Technologies (Coralville, IA, US). Single-strand oligonucleotides were also purchased from Integrated DNA Technologies.

2.2. Samples preparation

Substrates were first cleaned with acetone, ethanol and isopropanol and blow dried under nitrogen stream. To remove any carbon contaminants they were then exposed to oxygen plasma (80 mTorr, 15 sccm O_2, 20 W) in a reactive ion etching system (Plasmatherm 790 RIE) for duration of 3-5 min.

2.3. Atomic force microscopy (AFM)

The nanopatterned template was investigated by Agilent 5100 AFM system (Santa Clara, CA, US) and aluminium coated silicon probes (PPP-NCHR) obtained from Nano And More (Paris, France). Topographical images were acquired by AFM in tapping mode at 3.2 V tapping voltage on an area of 2–4 μm. Height, diameters and pitches were extracted using Gwyddion 2.55 and Nanoscope Analysis. Heights distributions used in the template fabrication for oligonucleotides experiments were fitted to extracted histograms using OriginPRO 2019b.

2.4. Scanning electron microscopy (SEM)

SEM images were acquired using Helios 650 FE-SEM (Hillsboro, OR, US), at accelerating voltage between 2 and 5 KV and beam current of 25 pA in top-view mode. The measurements were performed at multiple areas across the nanopatterned sensors to ascertain pattern integrity.

2.5. Nanopatterns for AuNP adsorption

The unpatterned control was prepared by immersing gold-coated quartz crystal in amino-thiol (4-ATP, or 4-VPT) solution (5 mM in ethanol) for > 16 h typically, then washed and blow dried. The micellar template was obtained by a process reported earlier [24,25]: PS-*b*-P2VP of System A (diluted concentration between 0.5% and 1.4% w/v in m-xylene) was spin-coated on QCM sensor at fix spin speeds of 6000 RPM. [26] Different periodicities were obtained by different block copolymer concentration. The surface as coated was then exposed to reactive ion etching for 30 s using oxygen plasma. Gold nanoparticles (AuNPs) were produced in-house using sodium citrate as reducing and stabilizing agent, according to Turkevich's method. [27–29] Gold colloids were characterized in size using SEM image analysis '($d = 10.9$ +/- *0.75 nm)*', and in pH = 6.8. QCM sensors with proper functionalization or template were then mounted in a QCM open module (QFM 401, Biolin Scientific, Sweden) which allows the injection of liquid directly on the sensor. The solution with gold nanoparticles was pipetted on top of the QCM sensor after a stable baseline was reached (refer to section 2.7 for QCM methods). The adsorption was left to occur for 3 h after which the substrate was washed repeatedly with water and dried in-situ, at the end of the process the adsorbed mass was measured.

2.6. Single strand oligonucleotides preparation and experimental protocol

Single strand probes and targets were diluted down to desired concentration in IDTE + 0.5 M NaCl buffer. The same buffer has also been used for the washing steps between the various injection in the experimental protocol. The probe is a 20 bp sequence with a molecular weight of 6443.4 g/mol (TGC CCT ATT GTT GCG TCG GA), consisting of thiol end group to enable binding to gold surface. To the probe solution a 100x molar excess of (tris(2-carboxyethyl) phosphine) (TCEP) was added to ensure that all the probes exist singularly and that no disulphide bond is present in the mix. The target contains the complementary sequence of the probe to ensure the correct match (AA AAA AAA AAA AAT CCG ACG CAA CAA TAG GGC A) and is 33 bp sequence with molecular weight of 10724.4 g/mole. The secondary oligonucleotide solution is prepared only at 1 μM in IDTE + 0.5 M of NaCl. Experimentally, the pursued concentration of primary probe (thus the probe chain and TCEP 100x molar excess together) is injected after a stable baseline has been achieved with IDTE + 0.5 M NaCl only. After 60 min of continuous injection at 20 μL/min, the surface is again equilibrated in buffer. Before injecting the target oligonucleotides chain, the buffer is switched to nuclease-free water and a solution of 6-mercapto-1-hexanol (MCH, 1 mM in nuclease-free water) is injected until saturation. Surface is again washed with nuclease-free water and the circuit buffer is switched back to IDTE + 0.5 M NaCl to ensure the correct environment for the target oligonucleotides chain hybridization. Target injection lasts for 60 min, buffer is again flushed over the substrate afterwards.

2.7. Quartz crystal microbalance (QCM)

QCM measurements with dissipation monitoring (QCM-D) was acquired using QSense Analyzer system (Biolin Scientific, Sweden). The QCM-D system was coupled with both an open module (QOM 401) for gold nanoparticles experiment and a flow module (QFM 401) for molecular interaction experiment. The frequency shifts were converted to mass using Sauerbrey's equation, using 9th overtone for all data. The validity of the Sauerbrey's equation to obtain the adsorbed mass, was assured through low values of dissipation, which confirms the rigidity of adsorbed layers. $\Delta D/(\frac{\Delta f}{n}) \ll 0.4 \times 10^{-6} Hz^{-1}$.[30].

2.8. Surface plasmon resonance (SPR)

SPR measurements were acquired using MP-SPR 220 A Naali (DBA Bionavis, Tampere, Finland). SPR was used to measure density of OEG layers. The SPR sensor was immersed in the OEGs solution at 1 mM concentration in milli-Q water for a duration of 2 h followed by washing with milli-Q water. The angular shift was determined from the difference of SPR dip at 670 nm, before and after the OEG functionalization, and using the conversion factor, $1 mdeg = 0.8$ ng/cm^2. [31] The SPR was chosen, instead of the QCM, to measure the grafting density of OEGs to remove the uncertainties naturally encountered when the QCM is used to measure hydrophilic polymers. [32] To achieve the same surface grafting density on the QCM substrates, the process is maintained equal in terms of OEGs concentration, incubation time and surface activation protocol.

3. Results and discussion

3.1. Impact of miniaturized active areas on adsorption of AuNPs

Binary nanopatterns that enable selective adsorption onto nanoscale regions were prepared using self-assembled copolymer colloidal templates on surface. This approach, already covered in earlier publications, has been shown to be a promising and reliable technique to realize high-density nanoscale features spanning large areas of any desired surface. [33,34] The low standard deviation of the templates allowed the dimensions of the features and the feature densities to be defined within a tolerance of 15%. This allows the adsorption area to be readily calculated and correlated with adsorption outcome obtained from quartz crystal microbalance (QCM) measurements. The first part of this investigation is focused on investigating the impact of nanopatterns on the densities and kinetics of adsorption of a generic nano-object, namely, gold nanoparticles (AuNPs) (section 3.1). The second part focuses on investigating the impact of high density nanopatterns on the adsorption of oligonucleotides and their binding with complementary sequence (section 3.2).

3.1.1. Impact of nanopatterns on enhancement of density and kinetics of adsorption

Nanopatterns presenting a quasi-periodic, hexagonal array of positively charged templates were obtained directly on a QCM sensor using self-assembly of amphiphilic block copolymer reverse micelle colloids formed out of polystyrene-block-polyvinylpyridine. The presence of PVP renders the features positively charged at near-neutral pH,thereby driving attachment of negatively charged citrate-gold nanoparticles from an aqueous solution via electrostatic attraction. The attachment of the nanoparticles occurs only on the features, and thus presenting an interesting approach to investigate the influence of confinement on the adsorption outcome. The impact due to nanopatterns is compared with respect to unpatterned counterparts, that present positively charged amine SAMs. Two different controls were considered, viz. 4-aminothiophenol (4-ATP) containing a primary amine and 4-vinylpyridine thiol (4-VPT) presenting a tertiary amine. The Fig. 1 shows the height maps of the templates and the unpatterned counterparts made of 4-ATP SAMs, before and after adsorption of gold nanoparticles. The AFM images confirms the adsorption occurring to be restricted only to the features, with adsorption of gold nanoparticles resulting in a height increase that is consistent with expectation from the diameter of the gold nanoparticles (d = 10.9 +/- 1.3 nm). The AuNPs assembly on the template features can be assumed to be a monolayer, which is consistent with the observation from FESEM measurements. By characterizing the surface geometry with atomic force microscopy (AFM) it is possible to accurately derive the percentage of surface available for adsorption on the nanopatterned surface. The unpatterned surface is considered to have 100% of its surface available for adsorption. Depending on the specific block copolymer employed and coating conditions used, it is possible to vary the size and density of features, thereby obtaining different values for the percentage surface available (listed in Table 1). The surface available in case of nanopatterns is calculated as in Eq. 1.

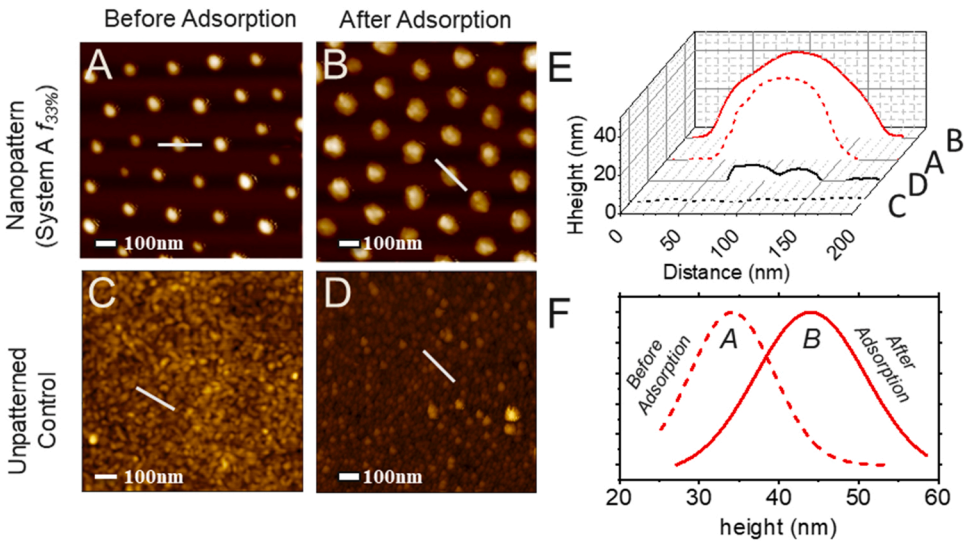

Fig. 1. Adsorption of AuNPs on nanopatterns versus unpatterned controls. **(A, D)** AFM images comparing **(A, B)** nanopatterned and **(C, D)** un-patterned QCM sensor surface, **(A, C)** before and **(B, D)** after attachment of gold nanoparticles. **(E)** line profiles corresponding to the white line segments in the AFM images shown in (**A-D**). **(F)** evolution in height distribution of the template features before and after AuNPs adsorption. **(E,F)** Dashed and solid lines indicate geometries before and after adsorption respectively. Red and black curves represent nanopatterns and unpatterned controls respectively.

Table 1
Geometric characteristics of the nanopatterns A and B used to investigate AuNPs adsorption. The subscripts in the pattern labels indicate fill factors. The molecular weight (M) of block copolymers or 4-ATP, the experimentally determined values for height (h), pitch (p), and feature density (f) and estimated values from Eq. 1 for surface per feature ($S_{feature}$) and actual surface area available ($S_{available}$) are provided.

Pattern label	M (Da)	h (nm)	p (nm)	f (/μm^2)	$S_{feature}$ (nm^2)	$S_{available}$ (%)
$A_{33\%}$	443 K	38.5	154	34	9780 + /- 10%	33%
$A_{61\%}$		38.5	111	66	9780 + /- 10%	61%
$B_{52\%}$	105 K	20	65	205	2513 + /- 10%	52%
$B_{58\%}$		20	61	233	2513 + /- 10%	58%
Unpatterned (4-ATP)	125.2	NA				100%

$$S_{available} = S_{feature} * f \quad (1)$$

Where $S_{feature}$ is the area of a single feature ($S_{feature} = 2\pi h^2$), where h is the height of the feature and f is the feature density per unit area. The calculation of the surface available is essential to obtain normalization factors that enables decorrelating the impact of the surface areas in the comparison between the adsorption responses of unpatterned and patterned surfaces.

To study the impact of nanopattern variables on the adsorption outcome, it is necessary to be able to fabricate nanopatterns with difference in the size and density of features. The size can be varied by changing the polymer molecular weight, while the change in fill factor is achieved by controlling the evaporation speeds during deposition of colloids. Table 1 summarizes 4 different patterns, constituting 2 different template sizes, with 2 different fill factors for each template size, that was used for the investigation. The values for height (h), pitch (p) and surface density of features (f) are determined using AFM and FESEM measurements, which are used to estimate the surface area available for adsorption, and the surface fill factors using Eq. 1. Fig. 2 compares the response of AuNPs adsorption on to pattern A with that of 2 different unpatterned control surfaces. The density and kinetics of adsorption was monitored using QCM. For these measurements, the QCM open module was used, which allows directly pipetting the solution on to the sensor surface. The sensor is first equilibrated in air, then exposed to 400 μL of AuNPs solution for duration of two hours followed by washing with milliQ water and drying before the frequency shift is recorded. The sensor frequency shift was converted to mass using Sauerbrey equation (cf. Methods). From the mass changes, it is possible to calculate the number of NPs per surface unit (NPs/μm^2) using Eq. 2.

$$[AuNP] = \Delta m/(V_{NP}\rho_{Au}) \quad (2)$$

Where Δm is the mass shift obtained from the frequency shift through the Sauerbrey's equation, V_{NP} is the estimated volume occupied by a single AuNP with a diameter $d = 10.9 + /- 1.3$ nm (Fig. S1) and $\rho_{Au} = 1.932ng/\mu m^3$ is the gold density.

The confirmation of the AuNPs distribution obtained after 2 h of incubation in AuNPs solutions was performed using FESEM measurements. The QCM measurements reveal an increasing trend for saturated AuNPs densities in the order of 4-VPT < 4-ATP < $A_{33\%}$ < $A_{61\%}$. The 4-VPT was used as a control that is representative of the PVP units used for the patterns. The adsorption of AuNPs to 4-ATP recorded a greater density of particles as compared to 4-VPT, yet comparable in terms of AuNPs surface coverage to other instances in literature. [35,36] The 4-ATP was chosen as a unpatterned control to compare the impact of nanopatterned surfaces. The density of AuNPs on $A_{33\%}$ was found to be almost similar to that of 4-ATP controls, while the density of $A_{61\%}$ was clearly over twice the density recorded on $A_{33\%}$. The observed density of AuNPs on the nanopatterns arises from adsorption to a fraction of the surface (33% or 61% for $A_{33\%}$ and $A_{61\%}$ respectively) as compared to unpatterned counterparts. Thus, a fair comparison between the surfaces cannot be made unless the available surface areas have been considered. Fig. 2**B** shows plots normalized with the available surface area. The comparison of the AuNPs density per unit area of the available surface reveals a dramatic enhancement on the nanopatterns as compared to the unpatterned counterparts. Further, Fig. 2**B** shows that the two patterned interfaces would reach the same AuNPs density (with a difference of 5.6% in their saturated densities). By considering the figures provided in Fig. 2**B**, the AuNPs surface coverage would reach the 46% and 48% of the surface for $A_{33\%}$, and $A_{61\%}$ respectively, while only 14% for the unpatterned 4-ATP SAM.

Conversion of mass changes to adsorption densities on surface can result in overestimation of mass arising out of hydration on surface bound films. [28] To factor this in, the QCM measurements were recorded both in presence and in absence of water on the sensor surface (see Fig S3). The results show that the hydration of the interface result in an overestimation of 17% in case of unpatterned interface, while 40% and 11% overestimation in case of $A_{33\%}$ and $A_{61\%}$ respectively. The AuNPs densities were in parallel determined using FESEM

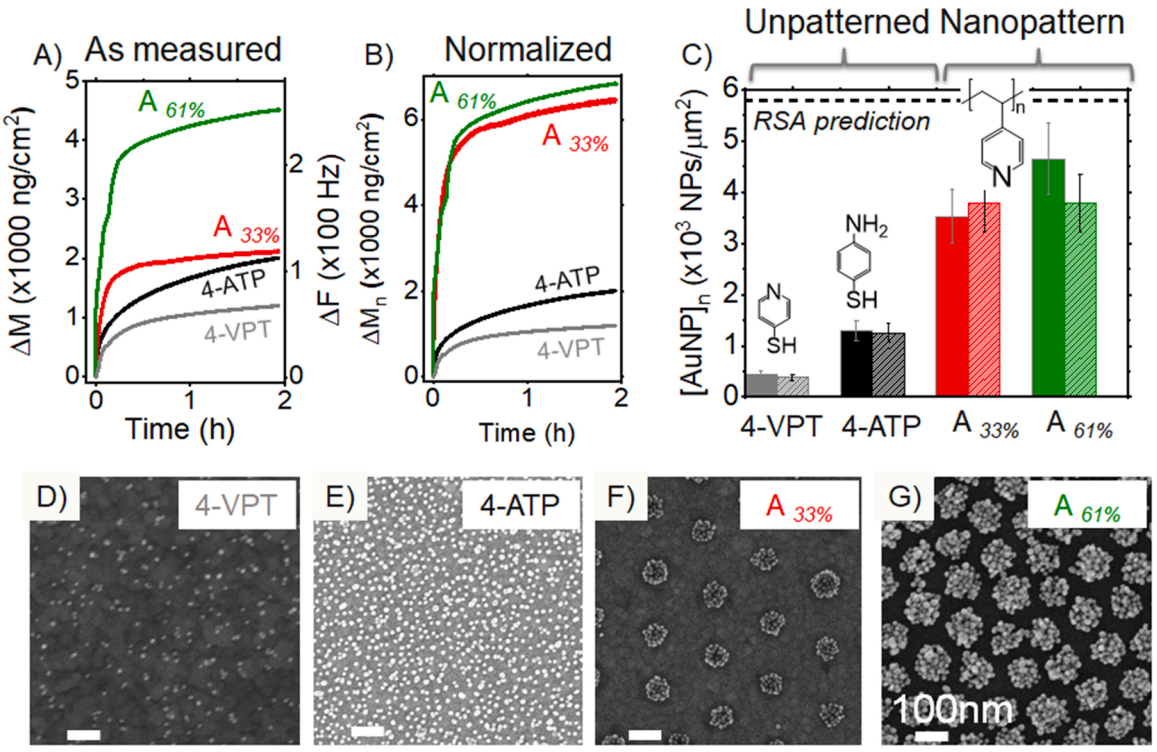

Fig. 2. **(A)** Kinetics of AuNPs adsorption on nanopatterns ($A_{33\%}$, black curve – $A_{61\%}$, green curve) and unpatterned control (on 4-ATP, red curve – on 4-VPT, grey curve) **(B)** shows the data normalized to the relative surface available. **(C)** shows a comparison of normalized saturated density of adsorption for patterned surface at two different fill factors and the 2 unpatterned surfaces. The two datasets are in good agreement with each other. [NPs] is obtained by Eq. 1. (D-G) SEM micrographs of (D) 4-VPT, (E) 4-ATP, (F) $A_{33\%}$ and (G) $A_{61\%}$ are shown. (enlarged images presented in Fig. S2).
Textured bars indicated the data as obtained from SEM, untextured bars indicates the source of data being QCM.

measurements to confirm if the averaged parameters obtained from QCM could effectively represent the adsorption density. Fig. 2**C** compares normalized AuNPs densities ($[AuNP]_n$) obtained from QCM mass changes under dry conditions, with those determined using FESEM. The strong agreement between the QCM and SEM measurements indicate the NP distribution observed by SEM to be representative of the distribution across the macroscopic QCM surface. $A_{33\%}$ and $A_{61\%}$ exhibited 36 or 38 NPs per feature, amounting to difference of only 5%, which thus shows a lack of impact of the fill factor on the resulting nanoparticle densities. The increasing the fill factor from 33% to 61% results in scaling of the

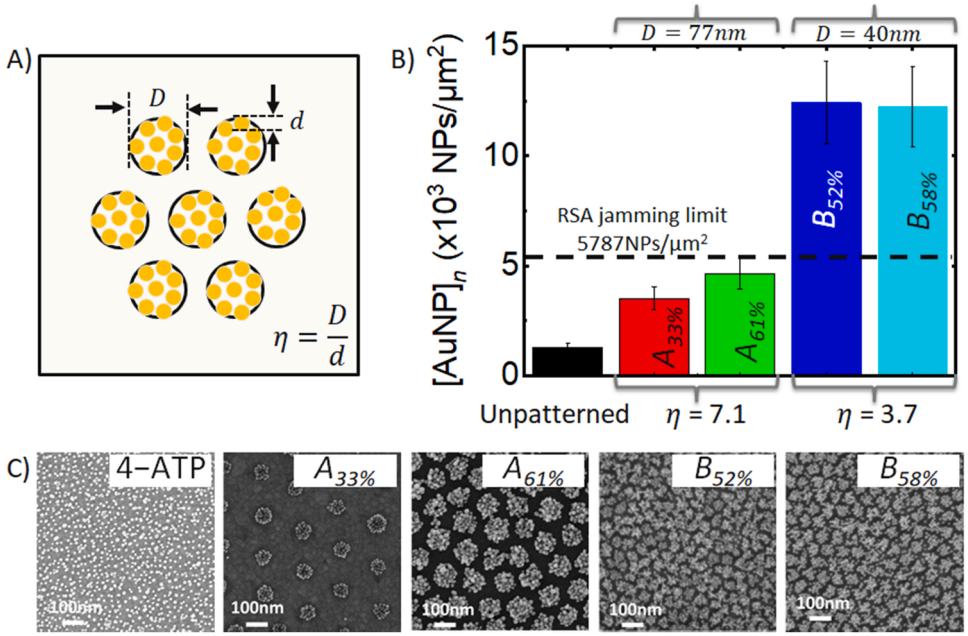

Fig. 3. Influence of the feature dimensions on the adsorption characteristics. (A) illustration of the relative dimensions of the nanopattern features and the nanoparticle, with the ratio of their diameters indicated by η. (B) Plot shows progressive increase in normalized AuNP densities with decreasing value of η. (C) The SEM micrographs of the corresponding surfaces in the plot is shown for reference. (enlarged SEM images presented in Fig. S2).

absolute signals intensities, proportional to the increase in feature densities in the nanopattern.

3.1.2. Impact of miniaturizing active areas on adsorption densities

Following the observation of the impact of nanopatterns and the influence of fill factors, we aimed at exploring the impact of the degree of confinement on the adsorption densities. An increase in the degree of confinement would be achieved with decrease in feature dimensions of the nanopatterns while maintaining the size of the nanoparticles. As shown in Table 1, the feature width of the nanopatterns was approximately halved while going from pattern A to pattern B. The reduced size results from the reduced dimension of the amphiphilic copolymer colloids, while going from copolymer of molecular weight of 443–105 kDa. The impact of the molecular characteristics of the copolymer on the micelle aggregation numbers and thereby their size have been reported elsewhere. [24] As for pattern A, the pattern B could also be produced with different fill factors, 52% ($B_{52\%}$) and 58% ($B_{58\%}$), by varying the evaporation speeds of the copolymer colloids during template formation. This allows the use of fill factors as an additional parameter while studying the impact of the feature widths.

FESEM images confirm the adsorption of AuNPs to be restricted to the polymer features in pattern B, as observed before for pattern A. (Fig. 3) On pattern B, the AuNPs adsorption was determined to be 12430NPs/μm^2 for $B_{52\%}$ and 12224NPs/μm^2 for the $B_{58\%}$ (after normalization). The relatively high surface coverage achieved of the order of 114–116% goes beyond possible physical explanation in terms of the standard RSA theory, which limits the maximum surface coverage to 54.7%. (dotted line, Fig. 3**B**) Other than the potential for non-specific nanoparticle binding that may occur between the features, potential multilayer adsorption could not be entirely ruled out on the basis of FESEM measurements. While the standard RSA theory disregards potential impact of the physical dimensions and shape on the nanoparticle coverage, other theories started to consider them to explain some of the outliers obtained experimentally where a surface coverage beyond 70% was achievable. [37–39] However, theories have yet to clarify any deviations from the RSA predictions in the scenario of random sequential adsorption occurring to a nanopatterned interface whose characteristic lengthscale is in the same order of magnitude of the approaching adsorbate. Independent of these considerations, there is clear enhancement in the attained densities as the width of the features that allow adsorption reduced from 7.1 (pattern A) to 3.7 (pattern B) multiples of the nanoparticle dimensions.

3.1.3. Nanopatterned adsorption under static conditions versus microfluidic flow- Indication of the role of analyte mass transport

It has been previously theoretically and empirically hypothesized that increased density and kinetics of adsorption on nanopatterned surface could be attributed to the enhanced analyte mass transport. [9, 10] A means to check the hypothesis would be to compare the performance of the nanopatterns in the presence and absence of an alternative influence such as convective flow that is also known to enhance analyte mass transport. Flow and other convection strategies are known to be effective ways to improve sensing performance especially in presence of low concentrations of analyte. In this direction, the AuNP binding response was compared for $A_{33\%}$ patterns and unpatterned surfaces in the absence (as in Section 3.1.2) and presence of flow. The flow experiments were performed by exposure of the nanopatterned and unpatterned surfaces to AuNP suspensions at a constant flow rate of 10 μL/min, for duration of ~2 h. Following the adsorption, the sensor was flushed with water, and the measurements of adsorption densities under water were taken into consideration. Comparison of the adsorption isotherms in the absence (Fig. 4, solid lines) and presence (Fig. 4, dotted lines) of flow shows a clear increase in the adsorption densities in the presence of flow for both unpatterned and patterned surface. To understand the impact of the concentration, the adsorption experiments were repeated for different concentrations of AuNP (within the range 2.1 pM - 21.1 nM), on nanopatterned and unpatterned surfaces, in the presence and absence of flow. (Fig. 5) It is also noteworthy to observe that while a nanopatterned interface is able to see a saturation plateau at similar concentration (around 2 nM), the unpatterned interface never sees the saturation in absence of flow. In the presence of the flow, both un-patterned and the patterned surfaces appear to reach saturation. The comparison of adsorption densities as function of concentration shows higher values for $A_{33\%}$ as compared to unpatterned samples for adsorption under both static and flow conditions. Moreover, it is possible to appreciate that at higher AuNPs concentration the difference between unpatterned and patterned substrate is reduced compared to lower concentration. The nanopatterns were able to sense as low as 200 pM compared to 5 nM possible for the unpatterned substrate for static conditions (Fig. 5A, C). The unpatterned surfaces could sense an order of magnitude better under flow, down to 20 pM of AuNPs.

Our findings suggest a better relative performance of the nanopattern as compared to unpatterned counterparts under static conditions as compared to under flow. The static conditions are especially valuable, as they can be easily realized under resource-constrained settings. The use of static conditions could obviate needs encountered for microfluidic conditions, viz. larger quantities of potentially precious samples, and more complex tools to handle small volumes. [40] In terms of normalized AuNPs surface coverage in static conditions, we see that $A_{33\%}$ shows a maximum surface density of 4012 NPs/μm^2 (corresponding to 37.4%) while the unpatterned surface reaches 662 NPs/μm^2 (6%) (Fig. 5**C**). Such surface coverage increases up to 7656 NPs/μm^2 (71.4%) for $A_{33\%}$ and up to 3129 NPs/μm^2 (29.2%) for the unpatterned substrate owing to the presence of the flow (Fig. 5**D**). The experiment shows both surfaces benefit from the introduction of convection with the nanopatterned surface doubling the NPs uptake and the unpatterned surface increasing it by a factor of five (Fig. 5**A-B**). The greater enhancement due to the flow on unpatterned samples as compared to the nanopatterns signifies a greater gain for the unpatterned surfaces. In other words, there is strong convergence in the effects due to introduction of nanopatterns and

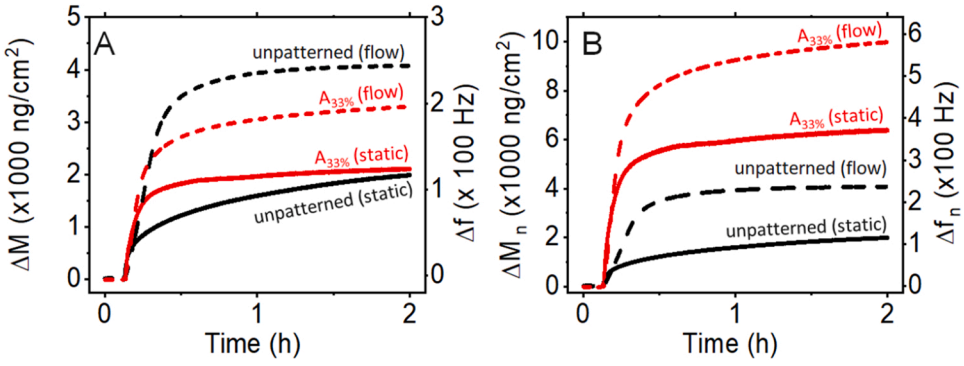

Fig. 4. Nanopatterned adsorption in the presence and absence of flow. **(A,B)** Adsorption isotherms for attachment of AuNPs on $A_{33\%}$ pattern (red curves) versus unpatterned controls (black lines) in the **(A)** absence (continuous lines) and **(B)** and presence of flow at 10 μL/min (dashed lines). **(B)** Adsorption on $A_{33\%}$ normalized to the available surface area (33%) for both the conditions evaluated. It can be seen that the presence of flow increases the absolute AuNPs adsorbed **(A)** and that the density of AuNPs is higher for the patterned template **(B)**.

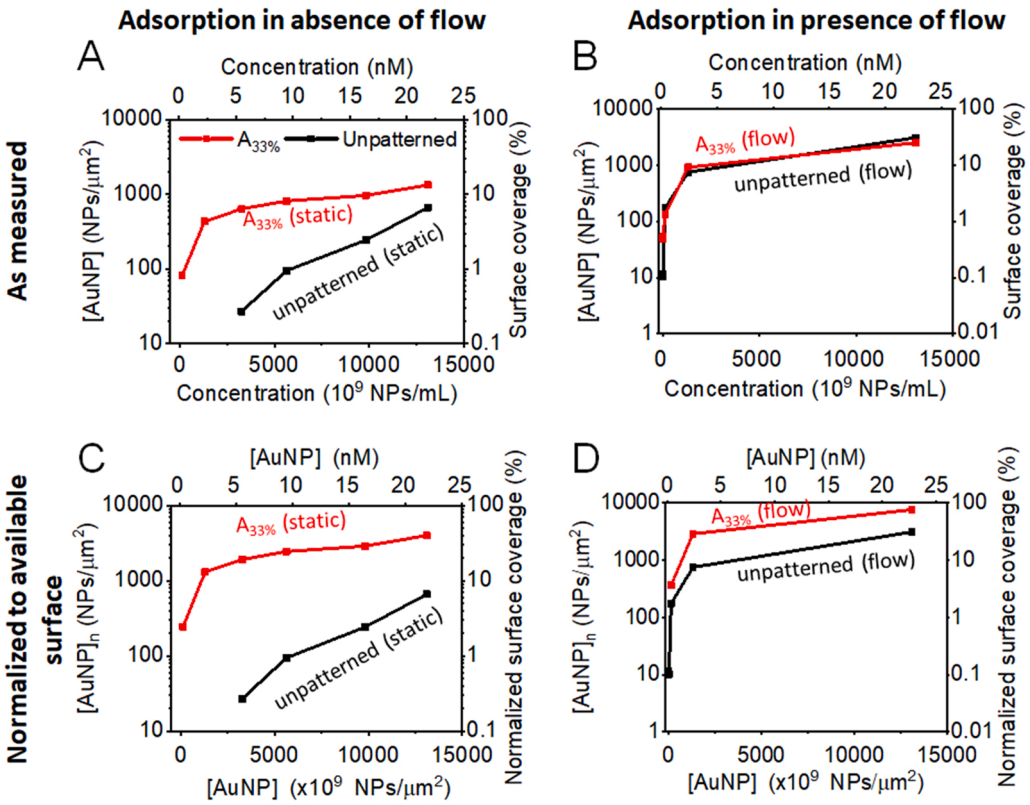

Fig. 5. Adsorption process obtained in absence of flow **(A)** and in presence **(B)**. The trend is also normalized by the respective surface area (i.e., 100% for the unpatterned surface and 37% for the patterned surface) in absence **(A)** and in presence of flow **(B)**. **(A)** and the normalized counterpart **(C)** are obtained by sequential injection of AuNPs solution.

convective flow towards enhancement in adsorption. Since an increase due to convective flow can be attributed to an increase in mass transport to the surface, [41] the findings strongly indicate the role of nanopattern towards enhancement in analyte mass transport to the surfaces.

3.1.4. Nanopatterns improve response times

The results so far have clearly shown the opportunity to enhance the density of nanoparticles adsorbed, through the introduction of nanopatterns with high fill factors, and with increasing degree of confinement. To understand the impact on the rate of adsorption, the time taken to reach an adsorption density equivalent to 90% of the saturated adsorption densities ($t_{90\%}$) attained on the unpatterned surface was compared for the different surfaces. (Fig. 6) Fig. 6**B** shows the nanopatterned surfaces to take only 1–3 min to reach an areal density equivalent to what is reached by the unpatterned surface in 70 min. The different nanopatterns thus take 1–4% of the time necessary to reach the same density as the unpatterned surface, for adsorption taking place under static conditions or under flow. There appears no impact of the fill factors on the response times. However, there appears to be an increase in the $t_{90\%}$ values with an increase in the degree of confinement, which could potentially result from an increase in the competition for the adsorption sites due increased degree of confinement for B (with feature

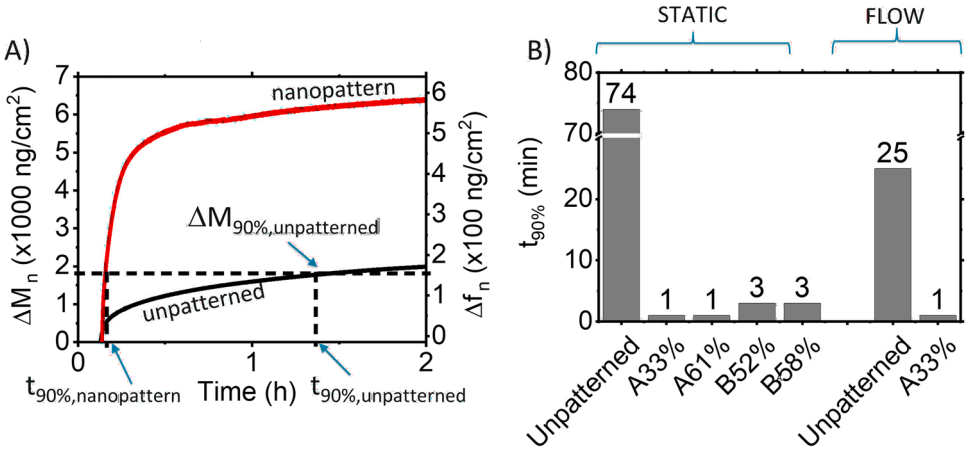

Fig. 6. Comparison of response times on nanopattern versus unpatterned counterparts. **(A)** Illustration of the means to arrive at the $t_{90\%}$, the time to attain an adsorption density equal to 90% of the saturated signal on unpatterned surface. **(B)** Plot of $t_{90\%}$, shown for 4-ATP SAMs, and the nanopatterns with the different fill factors and the degree of confinement, in the presence and absence of flow.

width ~50% that of A). Further, introduction of flow is found to result in a 3-fold decrease in the $t_{90\%}$ values of the unpatterned surface, while leaving that of $A_{33\%}$ unchanged. This is aligned with expectation of enhanced adsorption kinetics expected due to convective flow.

3.2. Impact of miniaturized active areas on adsorption of oligonucleic acids

3.2.1. Fabrication of nanopatterns with (bio)chemical contrast

The impact of nanopatterns on binding of nucleic acids was investigated, to see if an enhancement of adsorption is observed as in the case of AuNPs. These experiments require producing a nanopattern that restricts the binding of nucleic acids to pre-defined nanoscale regions on the surface. A schematic illustration of the fabrication sequence to produce nanopatterns with contrast in binding of nucleic acids is shown in Fig. 7. Briefly, block copolymer templates were formed out of PS-b-PVP with a molecular weight of 195 kDa-*b*-165 kDa, directly on the QCM sensor (Fig. 7**A(i)**). The templates were coated with Ti (5 nm)/Au (15 nm) to form a uniform gold surface with a periodic surface topography, as defined by the template underneath (Fig. 7**A(ii)**). The gold surface was then incubated overnight in an aqueous solution of oligoethylene glycol thiol (CH_3-EG_6-SH, OEG) and rinsed with water prior to use (Fig. 7**A(iii)**). The density of OEG SAMs were determined to be 1.89×10^{14} molecules/cm^2 (or 0.54 nm^2/molecule) by using SPR, by reproducing the OEG deposition on a SPR chip under identical conditions as for the gold topographies. The small size ($l = 2.5$ *nm*) and high densities of the OEG SAMs are expected to result in a brush configuration, allowing virtually no space for other molecules to diffuse in-between. [42] Upon deposition of the PEG, the surface does not show any type of contrast which would allow a selective molecular adsorption. In order to achieve such a contrast, we deployed a subtractive approach that removes the PEG selectively from the elevated regions of the surface. For this, the uniformly PEG functionalized topographic patterns were spin-coated with a solution of ZEP520A-7 (ZEP) in anisole to submerge the features. (Fig. 7**A(iv)**). The ZEP covered surface is subsequently etched using O_2 plasma RIE of either 90 s or 120 s for the patterns $C_{10\%}$ or $C_{24\%}$ respectively. The O_2 plasma RIE would remove the ZEP as well as the OEG SAM for part of the topography, with rate and duration that is programmed to leave 25 nm of the surface underneath unaffected (Fig. 7**A(v)**). The ZEP is subsequently removed with acetone to obtain a pattern of OEG SAM in the matrix, with bare gold exposed on the patches (Fig. 7**A(vi)**). The choice of ZEP as resist was made on basis of its specific characteristics of low degree of cross-linking induced by O_2 plasma that enables ease of removal by acetone, as well as assuring robust protection of OEG SAMs underneath .

3.2.2. Impact of nanopatterns on enhancement of adsorption and hybridization of oligonucleic acids

Two different patterns, namely $C_{10\%}$ or $C_{24\%}$ with exposed bare gold surface of 10% or 24% respectively, were obtained by starting from templates with feature density of 25 and 60 features/μm^2 respectively. The calculation of the available surface was made using the relevant parameters from AFM image analysis. Surfaces as processed show circular regions of bare gold in a continuous matrix of OEG. The nanopatterns with OEG contrast would direct any adsorption to occur selectively within the bare gold regions, due to the anti-fouling performance of the OEGs (experimentally tested to be > 98%, see Fig. S4a). A thorough characterization by AFM and SEM is performed before and after such process and a summary of the geometric characteristics of the nanopatterns is presented in Table 2. The nanopatterned QCM sensor surface was subsequently exposed to thiolated oligonucleotide probes to achieve selective attachment of the probe oligos to the exposed gold regions. Subsequently, the surface was exposed to the target oligonucleotide with complementary sequence. The probe and the target sequences were flown through a flow module, with a flow rate of 20 μL/min, for duration of 60 min each, followed by IDTE + 0.5 M NaCl buffer to establish a baseline.

Experiments were performed to identify the impact of solution concentration on the probe surface density, with each concentration performed independently on a freshly nanopatterned sensor. (Fig. 8**A-B**) As expected, the adsorption density of the probe oligos increases with the increase in its solution concentration. At the solution concentration of 1 μM, the unpatterned control recorded a mass density of 460 ng/cm^2 while the two patterned surfaces showed a mass density of 141 ng/cm^2 ($C_{10\%}$) and 194 ng/cm^2 ($C_{24\%}$). The mass density increases in the order $C_{10\%} < C_{24\%} <$ unpatterned surface, which is as expected based on the available surface areas. However, when normalized to the available surface, the $C_{10\%}$ and $C_{24\%}$ show density of 1410 ng/cm^2 and 808 ng/cm^2, which is clearly higher than the unpatterned surface by 306% and 175% respectively. (Fig. S4A) All throughout the concentration range studied, the $C_{10\%}$ is found to achieve higher density of probes compared to both $C_{24\%}$ and the unpatterned surface, while the difference increases at higher probe solution concentrations. The lower molecular densities at higher fill factors is aligned with theoretical studies that an increase in fill factor may not be necessarily advantageous in terms of achievable molecular densities. [9] In the next step, the probe functionalized surfaces obtained were exposed to target strands at a fixed concentration to follow the hybridization. Before exposure to the target sequence, the

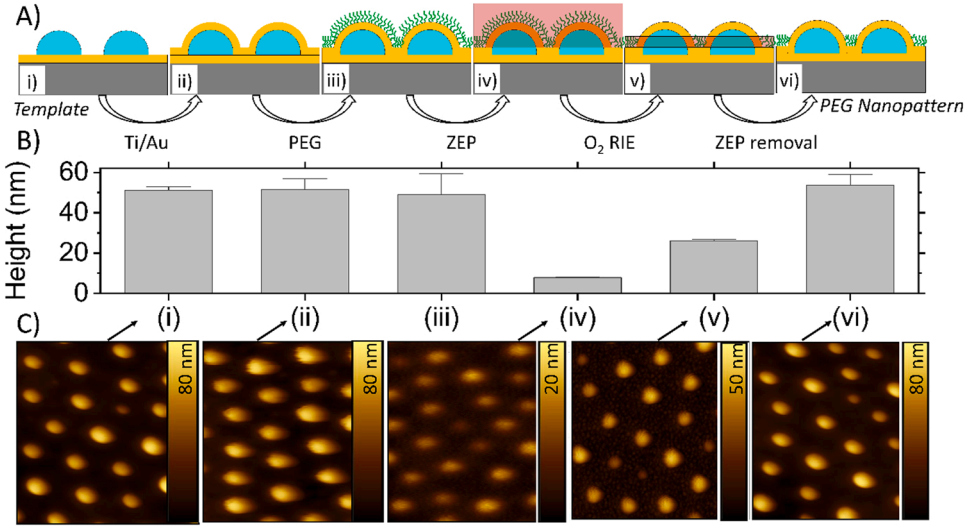

Fig. 7. Fabrication and characterization of OEG nanopatterns. (**A**) Schematic illustration of the fabrication workflow. **(i)** polymer templates on QCM sensors, subjected to **(ii)** evaporation of (5 nm) Ti/(15 nm) Au **(iii)** functionalization with OEG **(iv)** Spin-coating of ZEP resist to partially mask the surface features. **(v)** O_2 plasma RIE of controlled duration to expose the top of the features. **(vi)** Removal of ZEP to result in OEG nanopattern. (**B**) Corresponding feature heights as measured using AFM (**C**) AFM images of specific steps shown for reference.

Table 2
The geometric characteristics of the OEG nanopatterns (labelled as 'C') used for studying adsorption of oligonucleotides. The subscripts in the pattern labels indicate fill factors. The molecular weight (M) of the block copolymer used, the experimentally determined values for feature density (*f*), pitch (*p*), feature heights (*h*), radius (*r*), and estimated values for surface area per feature ($S_{feature}$), total surface area available for adsorption ($S_{available}$) are provided for the nanopatterns corresponding to the steps (ii) and (v) illustrated in Fig. 7.

Pattern Label	M (KDa)	f (/μm^2)	p (nm)	Au topography before ZEP coating (Fig. 7ii)			Au topography after patterning (Fig. 7v)			
				h (nm)	r (nm)	$S_{feature}$ (nm^2)	h (nm)	r (nm)	$S_{feature}$ (nm^2)	$S_{available}$ (%)
$C_{10\%}$	360	25	186	50	50	15708	26	26	3927	10%
$C_{24\%}$		60	120							24%
Unpatterned	NA									100%

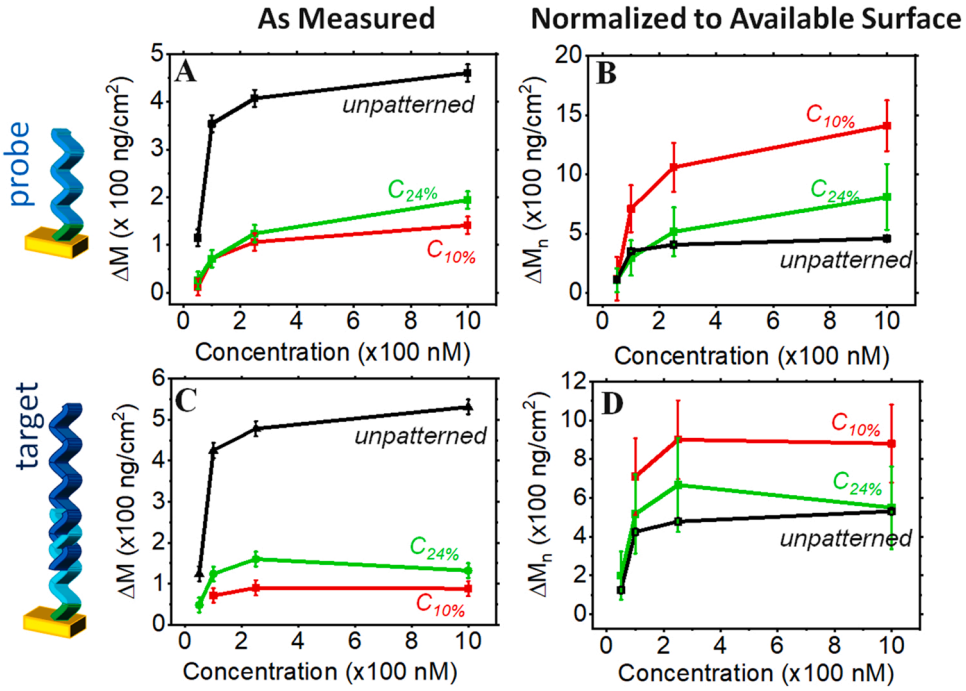

Fig. 8. Impact of nanopatterns on adsorption of oligonucleotides. **(A, B)** Adsorption of primary oligos (probe) to $C_{10\%}$ (red line) and $C_{24\%}$ (green line) and the unpatterned control (black line), shown (A) as measured and **(B)** upon normalization to the available surface (10% and 24%). **(C,D)** Adsorption of secondary oligonucleotides (target) to the probes, (**C**) before and **(D)** after normalization to available surface.

probe functionalized surface was washed in nuclease-free water and saturated with 6-mercapto-1-hexanol (MCH) to block non-specific binding sites. The higher surface concentration of probes resulted in higher densities of target capture (Fig. 8**C,** Fig. S4B). Upon normalization to the available surface, the target densities were also found to be distinctly higher as compared to unpatterned surface (Fig. 8**D**) The trends in Fig. 8**B** and Fig. 8**D** strongly suggests that a higher probe and target density is favoured at nanopatterns with lower fill factor. The molar ratios of the target to the probe would allow estimation of the hybridization efficiency as in Eq. 3.

$$\text{Hybridization } efficiency = \frac{\left(\Delta m_{target}/M_{target}\right)}{\left(\Delta m_{probe}/M_{probe}\right)} \quad (3)$$

Where Δm_{target} and Δm_{probe} are the mass density of the target and probe respectively and M_{target}, M_{probe} are the respective molecular weights (10724 Da and 6443 Da). The ratio describes the efficiency of hybridization: the closer the ratio is to *1* the higher the efficiency is. The hybridization efficiencies are compared for the nanopatterned and unpatterned surfaces as function of different probe surface concentrations.

The unpatterned surface shows a hybridization efficiency which is reasonably stable at 0.67 + /- 0.06. For nanopatterned surface the hybridization efficiency was found to correlate with the surface density of probes - a higher probe surface density was found to result in lower hybridization efficiency. This indicates an adverse impact of the receptor crowding that contributes to reducing the hybridization efficiency. (Fig. 9) Prior literature have shown that it is possible to achieve higher analyte surface density by engineering and minimizing the steric hindrance between adjacent receptor molecules.[43] We observed that for similar probe surface density the $C_{24\%}$ would always perform better than the unpatterned substrate. As a comparative example, at 0.1 μM of probe solution concentration $C_{24\%}$ and unpatterned surface have similar probe surface density (295 ng/cm^2 and 354 ng/cm^2 respectively) and thus we should obtain a similar ratio which however is equal to 1.05 for $C_{24\%}$ and of 0.72 for the unpatterned substrate. Concerning the $C_{10\%}$ nanopatterned interface we observed that the hybridization efficiency is constantly lower than the unpatterned counterpart. We estimated that the lower number of targets conjugated on $C_{10\%}$ (and $C_{24\%}$ to some extent) is strongly connected with the high probes surface density measured. Comparison of the response times were also made again, as for nanoparticles, as the time taken by the surfaces to reach 90% of the saturated adsorption density observed for the unpatterned surface. Results show the $C_{10\%}$ to be the quickest ($t_{90\%}$ of 4 min), followed by $C_{24\%}$ ($t_{90\%}$ of 12 min) and then by the unpatterned counterparts ($t_{90\%}$ of 16 min). (Fig S4 **C, D**) The $t_{90\%}$ in case of $C_{10\%}$ was found to be reduced by a factor of 4 compared to unpatterned surface, and a factor of 3 compared to $C_{24\%}$. Both patterns performed better than the unpatterned counterparts.

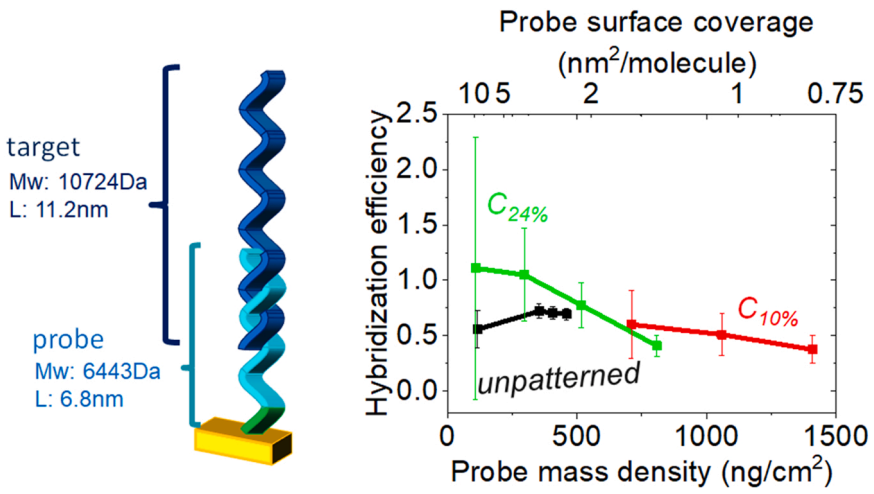

Fig. 9. Hybridization efficiency for nanopatterned versus unpatterned surfaces. Hybridization efficiency plotted as a function of the probe surface concentrations, for a fixed target concentration of 1 μM. The cartoon of the probe and the target along with their respective dimension is shown for reference.

While the behaviour of nanoparticles and oligonucleotides, towards adsorption on nanopatterned surfaces were found to be qualitatively similar, there were key differences. The greater density of the probe at lower fill factors, and the higher density of the target at lower probe surface densities are aspects that were observed only in case of oligonucleotide adsorption. The trends for response times match with what was observed for the adsorption of nanoparticles, yet, with enhancements for nanopatterns that are not as dramatic as presented in Fig. 6. The difference between nanoparticles and the oligos could stem from the isotropy of the nanoparticle surface with large number of equivalent surface sites with which it could bind to the aminated surface. The high surface density of ligands on the nanoparticle surface would increase its avidity, which in turn is known in literature to influence its binding response, and determine its fate in-vivo. [44] The behaviour is also similar to the virulence of the viruses that correlates with spike densities on their exterior surface. [45] The potential gains due to large number of equivalent surface sites on a nanoparticle surface could be an important, yet, less studied influence in several nanoparticle-based assays reported in literature. The oligos, on the other hand, have a specific binding configuration that is determined by the specificity of the complementary base pairing interactions. Although remaining to be tested, typical biospecific interactions would likely follow the behaviour of oligos when interacting with nanopatterns. The results provide interesting information on not only what to expect of the outcome of response with nanopattern but also provides some design tips on how to harness its benefits. The results also point to the potential opportunity to increase density and decrease response times by the use of ligand decorated nanoparticles in combination with nanopatterns with high fill factors.

4. Conclusion

Impact of confined adsorption within nanopatterns was investigated as a function of pattern fill factor, degree of confinement, presence of microfluidic flow, and the type of adsorbate. The impact of nanopattern geometry on adsorption response was compared for two different scenarios, viz., electrostatic binding of gold nanoparticles, and hybridization of oligonucleotides. Well-defined nanopatterns with desired geometric attributes were fabricated directly on QCM sensors enabling absolute, quantitative, and real-time information of the impact of nanopattern characteristics on the adsorption density and kinetics. The uniformity of the nanopatterns allowed ease of geometric modelling that enabled translating the macroscopic QCM signal to what occurred at the level of individual features. AuNPs density onto nanoscale features was found to be significantly enhanced on nanopatterns as compared to bare surface counterparts. The nanoparticle densities increased further with reduction in the size of the nanoscopic regions where adsorption occurred, or in other words, with increase in the degree of confinement. The increase in fill factors did not increase the density of adsorption within the nanoscale features, while contributed favorably by increasing the macroscopic sensor signal, proportionate to the feature densities. Findings also revealed a similarity in the influence of nanopatterns and convective flow towards enhancing the adsorption densities. This similarity supports the hypothesis that the enhanced adsorption within nanopatterns would result from enhanced analyte mass transport to the sensor surface. The increased rate of adsorption within nanoscale regions as compared to unpatterned counterparts further supports this hypothesis. The nanopatterned adsorption of oligonucleotides appears to exhibit qualitative similarities with that of nanoparticles, yet, with important differences. The oligonucleotide probes were found to adsorb at a greater density on nanopatterns with a lower fill factor, while revealing higher hybridization efficiency on the nanopatterns with higher fill factor. The differences between the adsorption responses of nanoparticles versus oligonucleotides may stem from large number of equivalent binding sites on the gold nanoparticles that increases its probability of adsorption, and the adverse impact of steric hindrance on the hybridization of oligonucleotides at high probe densities. The findings favour miniaturization of sensing footprints to length scales of the order of analyte dimensions with potential to bring performance incentives in combination with existing nanoscale sensors such as plasmonic nanoantennae, or nanowire FETs. The work further demonstrates nanopatterned QCM sensors as a unique and generic design tool to advance the investigations of nano-bio interactions for rational design of biosensors, and bio interfaces.

CRediT authorship contribution statement

Matteo Beggiato: Methodology, Writing – original draft, Visualization. **Christine Dupont**: Methodology, Writing – review & editing. **Rishabh Rastogi**: Methodology. **Sivashankar Krishnamoorthy**: Conceptualization, Supervision, Methodology, Visualization, Writing – original draft.

Declaration of Competing Interest

The authors declare the following financial interests/personal relationships which may be considered as potential competing interests: Sivashankar Krishnamoorthy reports financial support was provided by Luxembourg National Research Fund. Sivashankar Krishnamoorthy has

patent pending to Luxembourg Institute of Science and Technology.

Acknowledgements

Funding from Fonds National de la Recherche (FNR) Luxembourg via MASSENA and PLASENS (C15/MS/10459961) projects is gratefully acknowledged.

Appendix A. Supporting information

Supplementary data associated with this article can be found in the online version at doi:10.1016/j.snb.2022.131945.

References

[1] Y.A. Perez Sirkin, M. Tagliazucchi, I. Szleifer, Transport in nanopores and nanochannels: some fundamental challenges and nature-inspired solutions, Mater. Today Adv. 5 (2020), 100047, https://doi.org/10.1016/j.mtadv.2019.100047.
[2] W. Zhang, P. Gu, Z. Wang, B. Ai, Z. Zhou, Z. Zhao, C. Li, Z. Shi, G. Zhang, Integrated "Hot Spots": tunable sub-10 nm crescent nanogap arrays, Adv. Opt. Mater. 7 (2019) 1–8, https://doi.org/10.1002/adom.201901337.
[3] P.R. Nair, M.A. Alam, Performance limits of nanobiosensors, Appl. Phys. Lett. 88 (2006), 233120, https://doi.org/10.1063/1.2211310.
[4] A.B. Asha, R. Narain, Nanomaterials properties, Elsevier Inc, 2020, https://doi.org/10.1016/b978-0-12-816806-6.00015-7.
[5] H. Agheli, J. Malmström, E.M. Larsson, M. Textor, D.S. Sutherland, Large area protein nanopatterning for biological applications, Nano Lett. 6 (2006) 1165–1171, https://doi.org/10.1021/nl060403i.
[6] A. Valsesia, I. Mannelli, P. Colpo, F. Bretagnol, F. Rossi, Protein nanopatterns for improved immunodetection sensitivity, Anal. Chem. 80 (2008) 7336–7340, https://doi.org/10.1021/ac801021z.
[7] A. Valsesia, P. Colpo, I. Mannelli, S. Mornet, F. Bretagnol, G. Ceccone, F. Rossi, Use of nanopaatterned surfaces to enhance immunoreaction efficiency, Anal. Chem. 80 (2008) 1418–1424, https://doi.org/10.1021/ac701762k.
[8] S. Krishnamoorthy, M. Himmelhaus, Confinement-induced enhancement of antigen-antibody interactions within binary nanopatterns to achieve higher efficiency of on-chip immunosensors, Adv. Mater. 20 (2008) 2782–2788, https://doi.org/10.1002/adma.200702188.
[9] B. Špačková, N.S. Lynn, J. Slabý, H. Šípová, J. Homola, A route to superior performance of a nanoplasmonic biosensor: consideration of both photonic and mass transport aspects, ACS Photonics 5 (2018) 1019–1025, https://doi.org/10.1021/acsphotonics.7b01319.
[10] N.S. Lynn, J. Homola, Bio)sensing using nanoparticle arrays: on the effect of analyte transport on sensitivity, Anal. Chem. 88 (2016) 12145–12151, https://doi.org/10.1021/acs.analchem.6b03002.
[11] Q. Hu, C. Wu, Z. Dong, G. Zhang, Z. Ma, X. Wang, S. Sun, J. Xu, Direct confirmation of confinement effects by NiO confined in helical SnO2 nanocoils and its application in sensors, J. Mater. Chem. A. 10 (2022) 2786–2794, https://doi.org/10.1039/D1TA08630H.
[12] Z. Xue, C. Yan, T. Wang, From atoms to lives: the evolution of nanoparticle assemblies, Adv. Funct. Mater. 29 (2019) 1–33, https://doi.org/10.1002/adfm.201807658.
[13] B. Della Ventura, M. Iannaccone, R. Funari, M.P. Ciamarra, C. Altucci, R. Capparelli, S. Roperto, R. Velotta, Effective antibodies immobilization and functionalized nanoparticles in a quartzcrystal microbalance-based immunosensor for the detection of parathion, PLoS One 12 (2017) 1–14, https://doi.org/10.1371/journal.pone.0171754.
[14] Z. Zhu, Y. Ding, Z. Wang, C. Cheng, D. Li, H. Chen, High-performance plasmonic refractive index sensors via synergy between annealed nanoparticles and thin films, Nanotechnology 31 (2020), https://doi.org/10.1088/1361-6528/ab7531.
[15] G.J. Nusz, A.C. Curry, S.M. Marinakos, A. Wax, A. Chilkoti, Rational selection of gold nanorod geometry for label-free plasmonic biosensors, ACS Nano 3 (2009) 795–806, https://doi.org/10.1021/nn8006465.
[16] L. Xu, W. Ma, L. Wang, C. Xu, H. Kuang, N.A. Kotov, Nanoparticle assemblies: dimensional transformation of nanomaterials and scalability, Chem. Soc. Rev. 42 (2013) 3114–3126, https://doi.org/10.1039/c3cs35460a.
[17] S.J. Jeong, J.Y. Kim, B.H. Kim, H.S. Moon, S.O. Kim, Directed self-assembly of block copolymers for next generation nanolithography, Mater. Today 16 (2013) 468–476, https://doi.org/10.1016/j.mattod.2013.11.002.
[18] N. Asai, T. Shimizu, S. Shingubara, T. Ito, Fabrication of highly sensitive QCM sensor using AAO nanoholes and its application in biosensing, Sens. Actuators, B Chem. 276 (2018) 534–539, https://doi.org/10.1016/j.snb.2018.08.094.
[19] P.M. Mendes, S. Jacke, K. Critchley, J. Plaza, Y. Chen, K. Nikitin, R.E. Palmer, J. A. Preece, S.D. Evans, D. Fitzmaurice, Gold nanoparticle patterning of silicon wafers using chemical e-beam lithography, Langmuir 20 (2004) 3766–3768, https://doi.org/10.1021/la049803g.
[20] S.M. Park, X. Liang, B.D. Harteneck, T.E. Pick, N. Hiroshiba, Y. Wu, B.A. Helms, D. L. Olynick, Sub-10 nm nanofabrication via nanoimprint directed self-assembly of block copolymers, ACS Nano 5 (2011) 8523–8531, https://doi.org/10.1021/nn201391d.
[21] D. Wouters, U.S. Schubert, Nanolithography and nanochemistry: Probe-related patterning techniques and chemical modification for nanometer-sized devices, Angew. Chemie - Int. Ed. 43 (2004) 2480–2495. https://doi.org/10.1002/anie.200300609.
[22] G. Zhang, D. Wang, Fabrication of heterogeneous binary arrays of nanoparticles via colloidal lithography, J. Am. Chem. Soc. 130 (2008) 5616–5617, https://doi.org/10.1021/ja710771j.
[23] S. Krishnamoorthy, R. Pugin, J. Brugger, H. Heinzelmann, C. Hinderling, Tuning the dimensions and periodicities of nanostructures starting from the same polystyrene-block-poly(2-vinylpyridine) diblock copolymer, Adv. Funct. Mater. 16 (2006) 1469–1475, https://doi.org/10.1002/adfm.200500524.
[24] F.L. Yap, P. Thoniyot, S. Krishnan, S. Krishnamoorthy, Nanoparticle cluster arrays for high-performance SERS through directed self-assembly on flat substrates and on optical fibers, ACS Nano 6 (2012) 2056–2070.
[25] R. Rastogi, M. Beggiato, P.M. Adam, S. Juodkazis, S. Krishnamoorthy, Nanoplasmonic arrays with high spatial resolutions, Qual., Throughput Quant. Detect. Mol. Anal., Nanoplasmonic (2019), https://doi.org/10.5772/intechopen.89064.
[26] J.C. Meiners, A. Quintel-Ritzi, J. Mlynek, H. Elbs, G. Krausch, Adsorption of block-Copolymer micelles from a selective solvent, Macromolecules 30 (1997) 4945–4951, https://doi.org/10.1021/ma970327t.
[27] J. Turkevich, Colloidal gold. Part II, Gold. Bull. 18 (1985) 125–131, https://doi.org/10.1007/bf03214694.
[28] J. Turkevich, P.C. Stevenson, J. Hillier, A study of the nucleation and growth processes in the synthesis of colloidal gold, Discuss. Faraday Soc. 11 (1951) 55–75.
[29] J. Turkevich, Colloidal gold. Part I - Historical and preparative aspects, morphology and structure, Gold. Bull. 18 (1985) 86–91, https://doi.org/10.1007/BF03214690.
[30] I. Reviakine, D. Johannsmann, R.P. Richter, Hearing what you cannot see and visualizing what you hear: interpreting quartz crystal microbalance data from solvated interfaces, Anal. Chem. 83 (2011) 8838–8848, https://doi.org/10.1021/ac201778h.
[31] Handbook of Surface Plasmon Resonance, Royal Society of Chemistry, 2017. https://doi.org/10.1039/9781788010283.
[32] N. Kananizadeh, C. Rice, J. Lee, K.B. Rodenhausen, D. Sekora, M. Schubert, E. Schubert, S. Bartelt-Hunt, Y. Li, Combined quartz crystal microbalance with dissipation (QCM-D) and generalized ellipsometry (GE) to characterize the deposition of titanium dioxide nanoparticles on model rough surfaces, J. Hazard. Mater. 322 (2017) 118–128, https://doi.org/10.1016/j.jhazmat.2016.03.048.
[33] F.L. Yap, P. Thoniyot, S. Krishnan, S. Krishnamoorthy, Nanoparticle cluster arrays for high-performance SERS through directed self-assembly on flat substrates and on optical fibers, ACS Nano 6 (2012), https://doi.org/10.1021/nn203661n.
[34] M.H. Nurmawati, P.K. Ajikumar, R. Renu, S. Valiyaveettil, Hierarchical self-organization of nanomaterials into two-dimensional arrays using functional polymer scaffold, Adv. Funct. Mater. 18 (2008) 3213–3218, https://doi.org/10.1002/adfm.200800396.
[35] T. Zhu, X. Fu, T. Mu, J. Wang, Z. Liu, pH-dependent adsorption of gold nanoparticles on p-aminothiophenol-modified gold substrates, Langmuir 15 (1999) 5197–5199, https://doi.org/10.1021/la990081g.
[36] K. Kim, H. Ryoo, Y.M. Lee, K.S. Shin, Adsorption characteristics of Au nanoparticles onto poly(4-vinylpyridine) surface revealed by QCM, AFM, UV/vis, and Raman scattering spectroscopy, J. Colloid Interface Sci. 342 (2010) 479–484, https://doi.org/10.1016/j.jcis.2009.10.019.
[37] J. Zhao, S. Li, R. Zou, A. Yu, Dense random packings of spherocylinders, Soft Matter 8 (2012) 1003–1009, https://doi.org/10.1039/c1sm06487h.
[38] W. Man, A. Donev, F.H. Stillinger, M.T. Sullivan, W.B. Russel, D. Heeger, S. Inati, S. Torquato, P.M. Chaikin, Experiments on random packings of ellipsoids, Phys. Rev. Lett. 94 (2005) 1–4, https://doi.org/10.1103/PhysRevLett.94.198001.
[39] A. Baule, R. Mari, L. Bo, L. Portal, H.A. Makse, Mean-field theory of random close packings of axisymmetric particles, Nat. Commun. 4 (2013) 1–11, https://doi.org/10.1038/ncomms3194.
[40] L. Tang, H.J. Kwon, K.A. Kang, Theoretical and experimental analysis of analyte transport in a fiber-optic, protein C immuno-biosensor, Biotechnol. Bioeng. 88 (2004) 869–879, https://doi.org/10.1002/bit.20310.
[41] T.M. Squires, R.J. Messinger, S.R. Manalis, Making it stick: convection, reaction and diffusion in surface-based biosensors, Nat. Biotechnol. 26 (2008) 417–426, https://doi.org/10.1038/nbt1388.
[42] S. Chen, L. Li, C. Zhao, J. Zheng, Surface hydration: principles and applications toward low-fouling/nonfouling biomaterials, Polymers 51 (2010) 5283–5293, https://doi.org/10.1016/j.polymer.2010.08.022.
[43] M.S. Shchepinov, S.C. Case-Green, E.M. Southern, Steric factors influencing hybridisation of nucleic acids to oligonucleotide arrays, Nucleic Acids Res. 25 (1997) 1155–1161, https://doi.org/10.1093/nar/25.6.1155.
[44] A. Tsourkas, D.R. Elias, A. Poloukhtine, V. Popik, Effect of ligand density, receptor density, and nanoparticle size on cell targeting., Nanomedicine Nanotechnology, Biol. Med. 9 (2013) 194–201, https://doi.org/10.1016/j.nano.2012.05.015.Effect.
[45] A.M. Alkilany, L. Zhu, H. Weller, A. Mews, W.J. Parak, M. Barz, N. Feliu, Ligand density on nanoparticles: a parameter with critical impact on nanomedicine, Adv. Drug Deliv. Rev. 143 (2019) 22–36, https://doi.org/10.1016/j.addr.2019.05.010.

Matteo Beggiato completed his Masters from Politecnico di Torino in Italy in 2017 and obtained his PhD degree from the University of Luxembourg, and Luxembourg Institute of Science and Technology in 2021. His PhD thesis focused on investigating Nanoengineered Interfaces to Enhance Analyte Mass Transport and Analyte Capture - Towards High Performance Affinity Biosensors. He is now a member of staff of IMEC, Belgium.

Rishabh Rastogi completed his Masters from Amity University in India in 2015 and his PhD degree from the University Technology of Troyes in France and Luxembourg Institute of Science and Technology in 2020. His PhD thesis focused on engineering electromagnetic hotspots for highly sensitive biomolecular detection by plasmon-enhanced spectroscopies. He is currently a member of staff of ASM, Belgium.

Christine Dupont received her PhD degree from UCLouvain, Belgium, in 2000. She has over 20 years of experience in physico-chemistry of interfaces, adsorbed protein layers, biomaterials science, cell-material interactions, nanobiotechnologies and biomimetic materials. She is currently a Full professor and Dean at the FFaculty of bioscience engineering and carries her research activities at the Institute of Condensed Matter and Nanosciences of UCLouvain.

Sivashankar Krishnamoorthy received his PhD degree from CSEM SA, Neuchatel, and EPFL, Switzerland, in 2006. He has over 18 years of experience in the research and development of advanced nanotechnologies in micro/nanofabrication, bio-interfaces, nanooptics and functional integration of engineered nanostructures within optical and electronic devices. He currently leads the group focused on nanoengineered biological devices and interfaces at the Luxembourg Institute of Science and Technology (LIST).